CHAPTER IV

THE NONEQUILIBRIUM ELECTRON-ELECTRON SCATTERING

In this chapter we study the nonequilibrium intersubband electron-electron scattering in detail. Specifically we evaluate for a complete upper-subband occupation below emitter chemical potential, $\mu_L \equiv \mu_2 + E_2$, the total scattering rate $\Gamma \equiv \Gamma_{22\to11}$ ($\Gamma_{22\to21}$) between two upper-subband electrons which both decay to the lower subband (of which only one decays to subband E_1) and estimate the resulting population inversion in the (hypothetical) Figure 1.1-tunneling structure.

We found in the previous Chapter III that the total *single*-electron intersubband decay, Γ_{se}, arising with the nonequilibrium current injection is at temperatures $T \leq 0.03$ meV bounded by decay rate, $1/\tau \approx 0.03$ meV, measured[1,2] at weak optical pumping of the corresponding *isolated* double-quantum-well structure.[3] If the total intersubband decay rate Γ_{nr}, where restricted to $\Gamma_{se} \approx 0.03$ meV, it would be straight forward to maintain the intersubband population inversion.

We find, however, a very significant *nonequilibrium* electron-electron scattering (Γ) whose strength can be deduced from measurements[1,2] of the equilibrium depolarization shift,[4,5,6,7] that is, the shift of the equilibrium absorption peak, Δ^*, from the subband separation, Δ. We furthermore find that the nonequilibrium scattering Γ is never significantly reduced by screening and, unlike the near-equilibrium electron-electron scattering,[8] is *not* inhibited by the Pauli exclusion principle (as we can assume population inversion.)

We consequently: (1) identify a simple scaling of the nonequilibrium electron-electron scattering Γ with the upper-subband occupation, (2) explain why the Pauli exclusion within the (assumed completely filled) upper subband prevents such a scaling for the other nonequilibrium electron-electron scattering rate $\Gamma_{22\to21}$, (3) identify a dramatic voltage-drop dependence of both nonequilibrium electron-electron scattering rates, Γ and $\Gamma_{22\to21}$, associated with the quantum-confined Stark effect[9] on the wavefunction inversion symmetry,[10] (4) document that this wavefunction-symmetry variation in particular allows a significant reduction of also the combined electron-electron intersubband decay, $\sim 2\Gamma + \Gamma_{22\to21}$, (5) predict a very strong decay rate $\sim 2\Gamma \approx 1$ meV for an upper-subband sheet-density $N_L \approx 10^{11}$ cm^{-2} comparable to that in the mid-infrared quantum cascade laser,[11,12,13] and finally (6) demonstrate that a smaller population inversion density ($\sim 0.2 \times 10^{11}$ cm^{-2}) *can* be maintained at a moderate tunneling current density.

The detailed outline of this chapter is as follows. In Section IV.A we introduce the intersubband Coulomb matrix element $U(q)$ which describes the $(2,2) \to (1,1)$ scattering Γ. We discuss both the unscreened and effectively screened interaction and explain how the strength of this interaction can be extracted from an experimental determination[1,2] of the depolarization shift.[4,5,6,7] In Section IV.B we demonstrate and explain an approximate scaling with electron occupation, μ_2/Δ, of the intersubband scattering rate Γ. In particular, we find the unscreened scattering rate is well approximated by a linear-in-μ_2 scaling result whereas, for the effectively screened interaction, we find some deviation. The effective screened causes, however, at most a factor-of-two reduction.

In Section IV.C we consider the other nonequilibrium intersubband electron-electron scattering $(2,2) \rightarrow (2,1)$. We evaluate the scattering rate $\Gamma_{22\rightarrow 21}$ assuming a complete upper-subband electron occupation below $\mu_L \equiv \mu_2 + E_2$ and we consequently include only the scattering events in which the final upper-subband state is located above μ_L and is thus available. For comparison we also evaluate the unscreened rate $\Gamma^*_{22\rightarrow 21}$ in which this Pauli exclusion effect is ignored. For the unscreened rate $\Gamma^*_{22\rightarrow 21}$ we find again an almost exact linear-in-μ_2 scaling result. However, for the scattering rate $\Gamma_{22\rightarrow 21}$ we find that the restrictions on the scattering phase space imposed by the Pauli exclusion principle prevents such a simple scaling even for the unscreened interaction.

In Section IV.D we predict a dramatic voltage-drop dependence of both Γ and $\Gamma_{22\rightarrow 21}$ which we explain based on the so-called quantum-confined Stark effect[9] on the wavefunction symmetry.[10] We show that the combined intersubband electron-electron decay rate ($\propto 2\Gamma + \Gamma_{22\rightarrow 21}$) enhances to a maximum at the avoided crossing, $V = V_{sym}$. Finally, in Section IV.E we provide a simple estimate for the resulting intersubband population inversion also at this avoided crossing. We demonstrate in particular, that a finite intersubband population inversion *can* be maintained in the Figure 1.1-tunneling structure in spite of the very strong nonequilibrium electron-electron scattering.

IV.A The effective intersubband Coulomb interaction

The intersubband scattering $(2,2) \to (1,1)$ involves, as illustrates in the top panel of Figure 1.1, two upper-subband electrons which both decay to lower subband E_1. For this intersubband electron-electron scattering, $(2,2) \to (1,1)$, the subband separation Δ defines a characteristic in-plane momentum transfer

$$q_\Delta = \sqrt{2m_e^* \Delta}, \tag{1}$$

in the intersubband electron-electron scattering rate $\Gamma \equiv \Gamma_{22\to 11}$. Together with the zero-frequency background dielectric constant ϵ_0, this characteristic momentum transfer provides a natural scaling of the effective Coulomb interaction,

$$V_{21,21}(q) \equiv \frac{e^2}{\epsilon_0 q_\Delta} U(q), \tag{2}$$

which describe an intersubband scattering event, $(2,2) \to (1,1)$, with in-plane momentum transfer q.

The effectively screened dimensionless matrix element $U(q)$ in Eq. (2) is defined

$$\begin{aligned} U(q) \equiv & U_{21,21}(q) = 2\pi \int dx_2 \int dx_1 \Psi_2(x_2)\Psi_1(x_2) \times \\ & q_\Delta \exp\left(-\sqrt{q^2+q_{TF}^2}|x_2-x_1|\right) / \sqrt{q^2+q_{TF}^2}\, \Psi_2(x_1)\Psi_1(x_1), \end{aligned} \tag{3}$$

in terms of the resonant-level wavefunctions[14] and Thomas-Fermi wave vector q_{TF} introduced below. The corresponding unscreened interaction matrix element $U^0(q)$ is given by the $q_{TF} \to 0$ limit of Eq. (3).

We observe that (even) the unscreened interaction matrix element, $U^0(q)$, is finite at $q = 0$. For the effectively screened $(U(q))$ and unscreened $(U^0(q))$ dimensionless matrix elements we furthermore find (a) a moderate q variation, (b) a correspondingly moderate dependence on the Thomas-Fermi screening wave vector $q_{TF} < q_\Delta$, and (c) a numerical value of $U^0(q = 0)$ that can be estimated from experiments.[2]

The moderate variation of $U^0(q)$ (point (a),) namely,

$$U^0(q_\Delta) \approx U^0(0)/4, \tag{4}$$

can be deduced analytically for a square quantum well with infinite barriers. Choosing the width, $L_0 \equiv \sqrt{3}\pi/q_\Delta$, of the quantum well to provide the actual subband separation Δ the unscreened dimensionless matrix element becomes

$$\begin{aligned} U^0_{sqw}(q) = 2\pi^2\sqrt{3}\Big[&A_1(qL_0) + A_1(qL_0) \\ &- 2qL_0(1 - e^{-qL_0})(A_1(qL_0) - A_3(qL_0))^2\Big], \end{aligned} \tag{5}$$

where

$$A_j(qL_0) = \frac{1}{(qL_0)^2 + (j\pi)^2}. \tag{6}$$

The value at $q = 0$ is $U^0_{sqw}(0) \approx 4$ whereas at $q = q_\Delta$ the unscreened matrix element reduces to $U^0_{sqw}(q_\Delta) \approx 1$.

Screening of the nonequilibrium electron-electron interaction, Eq. (3), is for simplicity treated within in an effective Thomas-Fermi approach defined by a corresponding *heated equilibrium* three-dimensional electron distribution. Specifically, the electron distribution within the tunneling region (having upper- and lower-subband occupation densities, n_1 and n_2, respectively) is described by an isotropic three-dimensional electron gas of density $n_{3D} = (n_1 + n_2)/L_{QB}$ at an elevated effective temperature, $1/\beta_{eff} = \Delta$. As an effective treatment of screening in the intersubband Coulomb interaction we use Eq. (3) the wave vector, q_{TF}, defined by this three-dimensional gas,

$$q_{TF}^2 = \left(\frac{4\pi e^2}{\epsilon_0 L_{QB}\Delta}\right)(n_1 + n_2). \tag{7}$$

As illustrated in top panel of Figure 1.1, a complete current-injected upper-subband electron occupation below the emitter chemical potential, μ_L, naturally defines a quasi-Fermi level

$$\mu_2 \equiv \mu_L - E_2, \tag{8}$$

and a corresponding wave vector

$$k_{\mu_2} \equiv \sqrt{2m_e^*\mu_2}. \tag{9}$$

This wave vector identifies the in-plane momentum of the most energetic of the current-injected states in the upper subband. The maximum upper-subband occupation density,

$$N_L = \frac{k_{\mu_2}^2}{2\pi} \propto \mu_2, \tag{10}$$

result with a complete occupation below this wave vector k_{μ_2}. Neglecting the lower-subband occupation ($n_1 \equiv 0$,) and assuming such a maximum upper-subband occupation, $n_2 = N_L$, we obtain the Thomas-Fermi wave vector

$$\begin{aligned} q_{TF} &= 2\left(\frac{\mathrm{Ry}^* a^*}{\Delta L_{QB}}\right)^{1/2} k_{\mu_2} \\ &\approx 0.9\, k_{\mu_2}, \end{aligned} \tag{11}$$

used in the effectively screened matrix element, Eq. (3).

Note that the Thomas-Fermi screening wave vector remains smaller than the characteristic momentum transfer, $q_{TF} < k_{\mu_2} \leq q_\Delta$ at $\mu_2 \leq \Delta$, even at $\mu_2 = \Delta$. That this effective Thomas-Fermi screening is ineffective (observation (b)) in modulating the nonequilibrium electron-electron scattering thus follows directly from the observation

$$U(q) = U^0(\sqrt{q^2 + q_{TF}^2}), \tag{12}$$

since we expect (observation (a)) only a moderate q-variation of $U^0(q)$ around $q = q_\Delta$.

Finally, the *strength* of the effective *nonequilibrium* electron-electron interaction, Eq. (2), is evident (point (c)) from the observed[1,2] large equilibrium depolarization shift[4,5,6,7] $\Delta^* - \Delta \approx 2$ meV of the absorption peak, Δ^*, from the far-infrared subband separation $\Delta \approx 11$ meV at sheet-density $N_s \approx 10^{11}$ cm^{-2}. In particular, neglecting the coupling to other quantum levels and assuming an inversion symmetry of the wavefunctions we have[6]

$$(\Delta^*)^2 - \Delta^2 = 2\Delta N_s(e^2/\epsilon_0 q_\Delta)U^0(q = 0). \tag{13}$$

For a finite occupation density $n_2 \lesssim N_L \sim N_s \approx 10^{11}$ cm^{-2} we thus expect the strong interaction $N_L(e^2/\epsilon_0 q_\Delta)U^0(0) \lesssim 2$ meV.

To motivate the relation, Eq. (13), we follow the discussion in Ref. 4 and consider the dynamic screening response of the double-quantum-well structure. Specifically, we describe the response of a sheet density N_s of electrons — initially located in lower level E_1 of quantum-well potential $\phi_{dc}(x)$ and described by wavefunction $\Psi_1(x)$ — to an external ac-field* $E_{ext} \exp(-i\omega t)$. This electric field results in a time-dependent potential $\phi_{ac}(x) \exp(-i\omega t)$. An approximate treatment of the dynamic screening results by assuming that $\phi_{dc}(x) \exp(-i\omega t)$ includes the self-consistent field arising from the electrons.

* Polarized in the $\hat{x}$- or growth-direction.

The time-dependent Schrödinger equation,

$$-i\frac{\partial}{\partial t}\Psi(x,t) = -\frac{1}{2m_e^*}\frac{\partial^2}{\partial x^2}\Psi(x,t) + e\left[\phi_{dc}(x) + \phi_1(x)\exp(-i\omega t)\right]\Psi(x,t), \qquad (14)$$

for the electron wavefunction, $\Psi(x,t)$, is formally solved to linear order in the potential $\phi_{ac}(x)$. Inserting this formal result in the Poisson equation,

$$\frac{\partial^2}{\partial x^2}\phi_{ac}(x)\exp(-i\omega t) = \frac{4\pi N_s e}{\epsilon_0}\left[|\Psi_1(x)|^2 - |\Psi(x,t)|^2\right], \qquad (15)$$

allows an analytical determination[4] of $\phi_{ac}(x)$ for a two level system.

Following Ref. 4 we introducing an effective length,

$$S_{22} = \int_{-\infty}^{\infty} dx \left(\int_{-\infty}^{x} dx' \Psi_2(x')\Psi_1(x')\right)^2, \qquad (16)$$

assume an effective absorption line-width, Γ_ϕ, and define the intersubband plasmon frequency ω_{ip} by

$$\omega_{ip}^2 \equiv \frac{8\pi N_s e^2}{\epsilon_0}\Delta S_{22}. \qquad (17)$$

The power dissipated within the entire quantum-well region can then be written[4]

$$P(\omega) = N_s e^2 |\langle\Psi_2|x|\Psi_1\rangle|^2 |E_{ext}|^2 \frac{\omega^2\Delta\Gamma_\phi}{(\omega^2 - \Delta^2 - \omega_{ip}^2)^2 + (\omega\Gamma_\phi)^2}. \qquad (18)$$

This power disspation describes in particular the frequency-dependent absorption from level E_1 to level E_2 which is peaked at a frequency

$$\Delta^* = \sqrt{\Delta^2 + \omega_{ip}^2} \approx \Delta + \frac{4\pi N_s e^2 S_{22}}{\epsilon_0}. \qquad (19)$$

This dynamical-screening effect results in the quantum-well structure investigated in Ref. 1,2 in the significant depolarization shift, $\Delta^* - \Delta \approx 2$ meV.

To establish the connection with the intersubband Coulomb interaction, expressed above in Eq. (13), we interpret the depolarization-shifted absorption peak, Eq. (19), as a collective node *identified* as a node of an effective dielectric constant. Specifically, while the actual self-consistent field does exhibit a spatial variation within the double-quantum-well potential (as a result of the dynamic screening[4]) we *can* define an *effective* dielectric function through

$$\langle\Psi_2|\Phi_{ac}|\Psi_1\rangle \equiv -\frac{E_{ext}}{\epsilon_{eff}(\omega)}\langle\Psi_2|x|\Psi_1\rangle. \tag{20}$$

Using the results for a two-level system (listed in in Ref. 4) we then have

$$\epsilon_{eff}(\omega) = 1 - \frac{4\pi e^2}{\epsilon_0}\chi_{12}^{0R}(\omega)S_{22}, \tag{21}$$

$$\chi_{12}^{0R}(\omega) = N_s\frac{2\Delta}{\omega^2 - \Delta^2 + 2i\delta\omega}. \tag{22}$$

Inserting this expression for $\epsilon_{eff}(\omega)$ in Eq. (18) we obtain

$$P(\omega) = N_s e^2|\langle\Psi_2|x|\Psi_1\rangle|^2\frac{|E_{ext}|^2}{\left|1 - \frac{4\pi e^2 S_{22}}{\epsilon_0}\chi_{12}^{0R}(\omega)\right|} \tag{23}$$

and the absorption peak, Eq. (19), coincides with the nodes of $\epsilon_{eff}(\omega)$.

We next observe that — for a symmetric potential (only) — the effective dielectric constant, $\epsilon_{eff}(\omega)$, is *identical* with the standard intersubband RPA-result[6]

$$\epsilon_{Inter}^{RPA}(\omega) = 1 - \left(\frac{e^2}{\epsilon_0 q_\Delta}\right)U^0(q\to 0)\chi_{12}^{0R}(\omega). \tag{24}$$

The equivalence between Eqs. (21) and (24) (for symmetric wavefunctions) can be expressed simply through the condition

$$4\pi q_\Delta S_{22} = U^0(q\to 0). \tag{25}$$

To verify the identity, Eq. (25), we observe that

$$\lim_{q\to 0} U^0(q) = -q_\Delta 2\pi\int_{-\infty}^{\infty} dx_2\int_{-\infty}^{\infty} dx_1\Psi_2(x_2)\Psi_1(x_2)|x_2 - x_1|\Psi_2(x_1)\Psi_1(x_1). \tag{26}$$

We furthermore rewrite the length, Eq. (16), according to

$$2S_{22} = -2\int_{-\infty}^{\infty} dx_1 \Psi_2(x_1)\Psi_1(x_1)\times \int_{-\infty}^{\infty} dx_2 \Theta(x_1 - x_2)(x_1 - x_2)\Psi_2(x_2)\Psi_1(x_2). \tag{27}$$

For a *symmetric* potential the identity Eq. (25) then follows simply by the inversion ($x_{j=1,2} \to -x_{j=1,2}$) within one of the two double-integrations in Eq. (27).

The equivalence between $\epsilon_{eff}(\omega)$ and the intersubband RPA-result $\epsilon_{Inter}^{RPA}(\omega)$, finally established the connection, Eq. (13), between the measured[1,2] equilibrium depolarization shift, $\Delta^* - \Delta$, and the intersubband Coulomb matrix element $U^0(q \to 0)$. Specifically, since the nodes of $\epsilon_{Inter}^{RPA}(\omega)$ are given by

$$(\omega^2 - \Delta^2) = \frac{e^2}{\epsilon_0 q_\Delta} U^0(q \to 0) 2N_s\Delta, \tag{28}$$

we obtain the following approximate expression for the depolarization shift

$$\Delta^* - \Delta \approx N_s \frac{e^2}{\epsilon_0 q_\Delta} U^0(q \to 0). \tag{29}$$

As previously stated, the large equilibrium depolarization shift, $\Delta^* - \Delta \approx 2$ meV observed[1,2] for a $N_s \approx 10^{11}$ cm^{-2} electron sheet density thus indicates a very significant *nonequilibrium* intersubband scattering Γ.

IV.B Scaling of nonequilibrium scattering Γ

The nonequilibrium current injection results, as illustrated in Figure 1.1, in a finite upper-subband electron occupation between E_2 and the emitter chemical potential μ_L. In contrast, the lower subband is only populated through intersubband decay processes. We shall here, using the Fermi golden rule, estimate the opposite-spin scattering rate[15] $\Gamma \equiv \Gamma_{22\to 11}$ assuming (a) a complete upper-subband occupation given by the quasi-Fermi level, μ_2, introduced in Eq. (8), and (b) a completely empty lower-subband. The second assumption (b) allows us to ignore the Pauli exclusion principle in our estimate of Γ since all final lower-subband states are available.

The scattering rate Γ arises from opposite-spin $(2,2) \to (1,1)$ scattering events with a finite in-plane momentum transfer q. The transition rate is given by the intersubband Coulomb matrix element, Eq. (2). Based on the formal derivation in Appendix A we obtain at zero temperature the following Fermi-golden-rule estimate[15]

$$\Gamma = \frac{\mathrm{Ry}^*}{\pi^2}\left(\frac{\mu_2}{\Delta}\right)\int \frac{dq}{k_{\mu_2}}|U(q)|^2 \; \left[(q/k_{\mu_2})P(q)\right]. \tag{30}$$

Here, $P(q)$, denotes a dimensionless phase-space contribution given by

$$N_L^2 \mu_2^{-1} P(q) = \tfrac{1}{2}\left(\frac{2}{A}\right)^2 \sum_{\vec{k},\vec{k}'} \Theta(\mu_2 - E_{||}(k))\Theta(\mu_2 - E_{||}(k'))2\pi\delta(E_f - E_i), \tag{31}$$

where A denotes the in-plane area of the structure and where the implied energy conservation reads

$$E_f - E_i = 2E_{||}(q) + \vec{q}\cdot(\vec{k} - \vec{k}')/m_e^* - 2\Delta. \tag{32}$$

The conservation of both in-plane momentum and energy, expressed in Eqs. (31) and (32), restricts the range of possible in-plane momentum transfers,

$$-1 \le q/k_{\mu_2} - \sqrt{1 + (q_\Delta/k_{\mu_2})^2} \le 1. \tag{33}$$

The domain, Eq. (33), of finite phase-space contributions, $P(q)$, also specifies the integration range in the estimate, Eq. (30). We observe in particular that the intersubband scattering always occurs at a finite in-plane momentum transfer $q > 0$.

The displayed factor one-half in the phase-space contribution Eq. (31) arises because we in this dissertation only consider the direct scattering between *opposite*-spin electrons. In addition to the opposite-spin scattering Γ there is of course also a same-spin scattering which comprises both a direct contribution ($\equiv \Gamma$) *and* an exchange contribution. However, we demonstrate in Appendix A that the direct and exchange contributions to the same-spin scattering exactly *cancel* if the interaction matrix element ($U(q)$) is independent of q. Because we expect just a moderate q-variation of the interaction matrix element (see Section IV.A) we restrict ourselves to evaluating alone the (dominant) opposite-spin direct scattering Γ.

The dashed-single-dotted curve in Figure 4.1 shows the (opposite-spin) scattering rate Γ evaluated from Eqs. (30), (31), and (32) using unscreened matrix element $U^0(q)$. The dashed-double-dotted curve in Figure 4.1 shows the scattering rate Γ evaluated using the effectively screened interaction matrix element $U(q) = U^0(\sqrt{q^2 + q_{TF}^2})$ defined by the effective Thomas-Fermi screening wave vector q_{TF} introduced in Section IV.A. We find that screening causes at most a factor-of-two reduction even at $\mu_2 = \Delta$.

The *solid* curve in Figure 4.1 demonstrates a linear-in-μ_2 scaling of the scattering rate Γ. This approximate scaling can be expressed

$$\Gamma \approx \frac{\mathrm{Ry}^*}{\pi^2} \left(\frac{\mu_2}{\Delta}\right) |U(q_\Delta)|^2 I_P(\mu_2/\Delta), \tag{34}$$

where

$$I_P(\mu_2/\Delta) \equiv \int \frac{dq}{k_{\mu_2}} \frac{q}{k_{\mu_2}} P(q) \approx I_P(0) = 0.785 \tag{35}$$

represent a dimensionless integrated phase-space measure essentially independent of μ_2/Δ. For the unscreened interaction (dashed-single-dotted curve) the linear

FIGURE 4.1 Approximate linear-in-μ_2 scaling, solid curve, of nonequilibrium scattering rate Γ estimated for a complete (current-injected) upper-subband occupation (between E_2 and emitter chemical potential $\mu_L \equiv E_2 + \mu_2$.) The dashed-single(double)-dotted curve shows the scattering rate Γ evaluated for the unscreened (effectively screened) intersubband Coulomb interaction matrix element $U^0(q)$ ($U(q) = U^0(\sqrt{q^2 + q_{TF}^2})$ defined by the screening wave vector $q_{TF} < q_\Delta$ introduced in Section IV.A) In Figure 4.2 we justify the scaling approximation, $\Gamma \approx (\mathrm{Ry}^*/\pi^2)(\mu_2/\Delta)|U(q_\Delta)|^2 I_P(0)$, given by the interaction matrix element evaluated at the characteristic momentum transfer, $q_\Delta = \sqrt{2m_e^* \Delta}$, and an almost constant dimensionless integrated phase-space measure, $I_P(\mu_2/\Delta) \approx I_P(0)$. The *solid* curve shows this scaling approximation evaluated for the unscreened interaction, i.e., using $U^0(q_\Delta)$. Comparing with the unscreened rate Γ (dashed-single-dotted curve) we find the predicted linear-in-μ_2 scaling is almost exact. For the effectively screened interaction (dashed-double-dotted curve) there is some deviation arising with the increased value of the Thomas-Fermi wave vector ($q_{TF}^2 \propto \mu_2$.) At most this screening causes a factor-of-two reduction even at $\mu_2 = \Delta$.

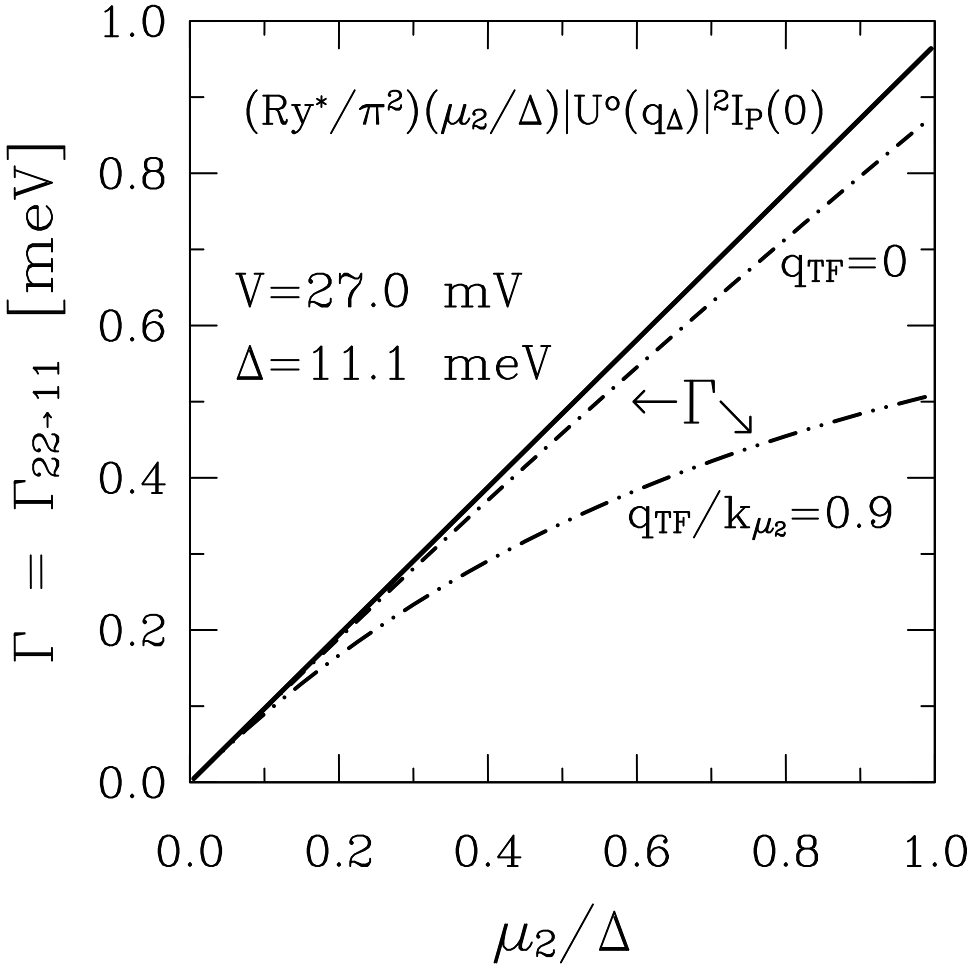

1.0
0.8
0.6
0.4
0.2
0.0
0.0
0.2
0.4
0.6
0.8
1.0
$\Gamma = \Gamma_{22\to11}$ [meV]
μ_2/Δ
$(\mathrm{Ry}^*/\pi^2)(\mu_2/\Delta)|U^o(q_\Delta)|^2 I_P(0)$
V=27.0 mV
Δ=11.1 meV
$q_{TF}=0$
$\leftarrow\Gamma_{\searrow}$
$q_{TF}/k_{\mu_2}=0.9$

FIGURE 4.1

scaling, Eqs, (34) and (35), is nearly exact. For the screened interaction there is some deviation arising from the decreasing value of the squared characteristic matrix element $|U(q_\Delta)|^2 = |U^0(\sqrt{q^2+q_\Delta^2})|^2$ with the enhanced Thomas-Fermi screening wave vector, $q_{TF} \propto k_{\mu_2}$, at higher electron occupation, μ_2/Δ.

The *middle* panel of Figure 4.2 demonstrates scaling of weighted dimensionless phase-space contribution, $(q/k_{\mu_2})P(q)$, and explains the result Eq. (35). In particular, we find this weighted phase-space measure, $(q/k_{\mu_2})P(q)$, (a) is restricted to a domain (Eq. (33)) with a μ_2/Δ-independent extension, (b) is always strongly peaked at the characteristic momentum transfer q_Δ resulting in the constant maximum value $(q_\Delta/k_{\mu_2})P(q_\Delta) = 8/(3\pi)$, and consequently (c) result in an almost μ_2/Δ-independent integrated phase-space measure, $I_P(\mu_2/\Delta) \approx I_P(0)$.

The key observation is (b) which follows from the assumed quadratic subband dispersion, $E_{||}(k)$. Specifically, the delta-function argument, Eq. (32), reduces at the characteristic momentum transfer, $q = q_\Delta$ (only,) to

$$E_f - E_i = q_\Delta(k_y - k'_y)/m_e^*, \tag{36}$$

where we have chosen the y-direction to be parallel to the in-plane momentum transfer $\hat{q}$. The phase-space contribution, given by Eq. (31), then scales as

$$N_L^2\mu_2^{-1}P(q_\Delta) = 4m_e^* k_{\mu_2}^3/2\pi^3 q_\Delta, \tag{37}$$

and (upon extracting $N_L^2\mu_2^{-1} = m_e^* k_{\mu_2}^2/2\pi^2$) we arrive at the predicted constant maximum value

$$(q_\Delta/k_{\mu_2})P(q_\Delta) = 8/(3\pi). \tag{38}$$

The observations (a)–(c) taken together justifies the central scaling approximation, Eqs. (34) and (37), *assuming* that the interaction matrix element $U(q)$ only

FIGURE 4.2 [Proof that no many-body theorist are needed here, *or*] Scaling with electron occupation, μ_2/Δ, of weighted phase-space contribution, middle panel, *and* unscreened (effectively screened) squared interaction matrix element, top (bottom) panel, describing the scattering rate Γ. The *middle* panel shows the weighted phase-space contribution, $(q/k_{\mu_2})P(q)$ (defined by $k_{\mu_2}^2 = 2m_e^*\mu_2$,) at different electron occupations. We find in the text (a) a constant extension of the scattering domain, $-1 \leq 1/k_{\mu_2} - \sqrt{1+(q_\Delta/k_{\mu_2})^2} \leq 1$, (b) a constant maximum value, $(q_\Delta/k_{\mu_2})P(q_\Delta) = 8/(3\pi)$ (indicated by horizontal dotted line,) at the characteristic momentum transfer $q_\Delta = \sqrt{2m_e^*\Delta}$, and consequently (c) an almost constant integrated dimensionless phase-space measure, $I_P(\mu_2/\Delta) \approx I_P(0) \sim 1$. The *top* (*bottom*) panel demonstrates that the (q/k_{μ_2})-variation of the squared unscreened interaction matrix element remains moderate at all μ_2/Δ. Because, furthermore, the weighted phase-space contribution is peaked at $q = q_\Delta$ we can approximate Γ using $|U^0(q)|^2 \approx |U^0(q_\Delta)|^2$ ($|U(q)|^2 \approx |U(q_\Delta)|^2$) for the unscreened (effective screened) interaction. This finally justifies the scaling approximation introduced in Figure 4.1.

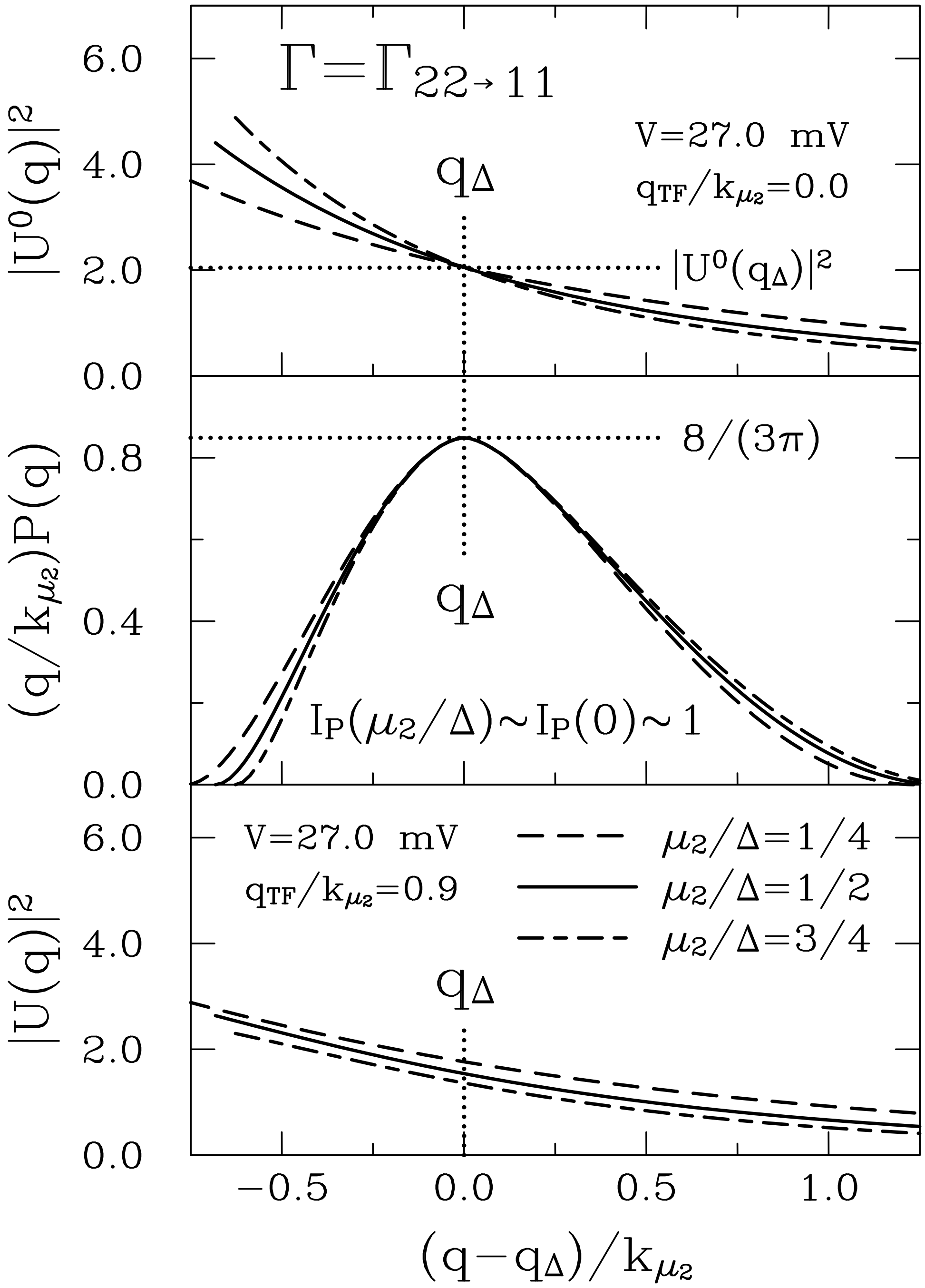
$\Gamma = \Gamma_{22\to11}$
V=27.0 mV
q_{TF}/k_{μ_2}=0.0
q_Δ
$|U^0(q_\Delta)|^2$
$|U^0(q)|^2$
6.0
4.0
2.0
0.0
8/(3π)
q_Δ
$I_P(\mu_2/\Delta) \sim I_P(0) \sim 1$
$(q/k_{\mu_2})P(q)$
0.8
0.4
0.0
V=27.0 mV
q_{TF}/k_{μ_2}=0.9
μ_2/Δ=1/4
μ_2/Δ=1/2
μ_2/Δ=3/4
q_Δ
$|U(q)|^2$
6.0
4.0
2.0
0.0
−0.5
0.0
0.5
1.0
$(q-q_\Delta)/k_{\mu_2}$

FIGURE 4.2

exhibits a moderate q-variation. In particular, since the scattering phase space in peaked at $q = q_\Delta$ we may then introduce the approximation $U(q) \approx U(q_\Delta)$ and obtain Eqs. (34) and (35).

The *top* panel in Figure 4.2 demonstrates that the q/k_{μ_2}-variation of squared unscreened matrix element $|U^0(q)|$ remains — at all electron occupations, μ_2/Δ — small within the domain of the phase-space contribution, $(q/k_{\mu_2})P(q)$. It also illustrates that the characteristic value, $|U^0(q_\Delta)|^2$, is a a good (weighted) average value of actual squared unscreened matrix element $|U^0(q)|^2$. The characteristic value, $U^0(q_\Delta)$, of the unscreened interaction is of course independent of the electron occupation, μ_2/Δ, which explains the almost exact agreement between the scaling result, Eq. (34), and the numerically evaluated estimate, Eq. (30), for the unscreened case — compare solid and dashed-single-dotted curves in Figure 4.1.

Similarly, the *bottom* panel of Figure 4.2 demonstrates that the q/k_{μ_2}-variation of squared, effective screened, interaction matrix element $|U(q)|^2$ remains small and can be approximated by $|U(q_\Delta)|^2$. This again motivates the approximation approximation Eqs. (34) and (35) also for the screened interaction — provided we use the effectively *screened characteristic* matrix element, $U(q_\Delta) = U^0(\sqrt{q_\Delta^2 + q_{TF}^2})$ (this approximation is not, however, evaluated in Figure 4.1.) That is, the deviation from a linear-in-μ_2 scaling for the interacting rate is primarily due to the increased screening of $|U(q_\Delta)|^2$ given by $q_{TF}^2 \propto \mu_2$.

IV.C The nonequilibrium scattering $\Gamma_{22\to 21}$

In addition to the scattering Γ, the nonequilibrium upper-subband current injection also results in a finite scattering $(2,2) \to (2,1)$ involving two upper-subband electrons of which only one decays to subband E_1. In this section we evaluate a Fermi-golden-rule estimate for the nonequilibrium electron-electron scattering rate $\Gamma_{22\to21}$ assuming again (a) a complete upper-subband electron occupation (of density N_L) below $\mu_L \equiv \mu_2 + E_2$, and (b) an empty lower subband E_1.

Because of the assumption (a) we must respect the Pauli exclusion principle within the upper subband. That is, in evaluating the rate $\Gamma_{22\to21}$ it is necessary to ensure that contributing scattering event has the final upper-subband state positioned above the emitter chemical potential $\mu_L = \mu_2 + E_2$. For comparison we also evaluate the scattering rate $\Gamma^*_{22\to21}$ in which we do not thus restrict the scattering phase-space.

The contribution to $\Gamma_{22\to21}$ from a scattering event $(2,2) \to (2,1)$ with in-plane momentum transfer q is described by the effective Coulomb interaction

$$V_{22,21}(q) = \left(\frac{e^2}{\epsilon_0 q_\Delta}\right) U_{12,22}(q) \tag{39}$$

In analogy with Section IV.A we have again introduced a scaling by $q_\Delta \equiv \sqrt{2m_e\Delta}$ and have thus define the dimensionless matrix element

$$\begin{aligned} U_{22,21}(q) =& 2\pi \int dx_2 \int dx_1 \Psi_2(x_2)\Psi_2(x_2)\times \\ & \frac{q_\Delta \exp\left(-\sqrt{q^2+q_{TF}^2}|x_2-x_1|\right)}{\sqrt{q^2+q_{TF}^2}} \Psi_2(x_1)\Psi_1(x_1). \end{aligned} \tag{40}$$

We assume the same effective screening as for the matrix element $U_{21,21}(q)$. That is, we use in Eq. (40) the Thomas-Fermi wave vector q_{TF} introduced in Section IV.A. Again the unscreened interaction matrix element, $U^0_{22,21}(q)$, results in the $q_{TF} \to 0$ limit of Eq. (40).

Based on a formal derivation provided in Appendix A we estimate the opposite-spin scattering at zero temperature using the following Fermi-golden-rule estimate[16]

$$\Gamma_{22\to 21} = \frac{\mathrm{Ry}^*}{\pi^2}\left(\frac{\mu_2}{\Delta}\right)\int \frac{dq}{k_{\mu_2}}|U_{22,21}(q)|^2\,\left[(q/k_{\mu_2})P_{22\to 21}(q)\right]. \tag{41}$$

In analogy with the discussion in Section IV.B we have in Eq. (41) introduced a dimensionless phase-space contribution, $P_{22\to 21}(q)$, defined by

$$\begin{aligned} N_L^2\mu_2^{-1}P_{22\to 21}(q) = \tfrac{1}{2}\,\frac{4}{A^2}\sum_{\vec{k},\vec{k}'}&\Theta(\mu_2 - E_{||}(k))\times \\ &\left[\Theta(\mu_2 - E_{||}(k'))\Theta(E_{||}(\vec{k}'-\vec{q}) - \mu_2)\right]\,2\pi\delta(E_f - E_i), \end{aligned} \tag{42}$$

where again A denotes the in-plane area of the tunneling structure.

In contrast to the discussion in Section IV.B, however, the condition for energy conservation in Eq. (42) now reads

$$E_f - E_i = 2E_{||}(q) + \vec{q}\cdot(\vec{k}-\vec{k}')/m_e^* - \Delta, \tag{43}$$

as only one electron decays to subband E_1. Also, the additional term, $\Theta(E_{||}(\vec{k}' - \vec{q}) - \mu_2)$, Eq. (42), restricts the final upper-subband state to be located above μ_L in accordance with the Pauli exclusion principle.*

The different condition, Eq. (43), for energy conservation and the restriction imposed by the Pauli exclusion principle modifies the scattering phase-space. We find that

$$q_{\Delta/2} \equiv \sqrt{2m_e^*(\Delta/2)} = q_\Delta/\sqrt{2}, \tag{44}$$

and not q_Δ itself, constitute the actual characteristic in-plane momentum transfer for $\Gamma_{22\to 21}$. Also, the phase-space domain, i.e., the range of possible in-plane

* The Pauli exclusion principle does *not* of course affect the rate $\Gamma \equiv \Gamma_{22\to 11}$ as all lower-subband states are assumed empty.

FIGURE 4.3 Electron-occupation dependence of nonequilibrium electron-electron scattering rate $\Gamma_{22\to 21}$ estimated for a complete (current-injected) upper-subband occupation (between E_2 and emitter chemical potential $\mu_L \equiv E_2+\mu_2$. In estimating $\Gamma_{22\to 21}$ we respect the Pauli exclusion within the upper-subband (only) and include only the scattering events in which the final upper-subband state is located above μ_L. The *dashed-dotted* curve shows the resulting estimate evaluated using the unscreened interaction described by intersubband Coulomb matrix element, $U_{22,21}(q)$. The *solid* curve shows the scattering rate estimated for the screened interaction, $U_{22\to 21}(q) = U^0_{22,21}(\sqrt{q^2+q^2_{TF}})$, where q_{TF} denotes the effective Thomas-Fermi screened wave vector introduced in Section IV.A. We observe that this effective screening (given by $q^2_{TF} \propto \mu_2$) again causes only a factor-of-two reduction even at $\mu_2 = \Delta$. In contrast to the scattering rate $\Gamma \equiv \Gamma_{22\to 11}$, however, we find that the Pauli exclusion within the upper-subband prohibits a linear-in-μ_2 scaling of even the unscreened scattering $\Gamma_{22\to 21}$. To illustrate this point the figure also shows the corresponding (unscreened) rate, $\Gamma^*_{22\to 21}$ (dotted curve,) in which we assume all final upper-subband states are available. Comparing unscreened scattering rates, $\Gamma^*_{22\to 21}$ and $\Gamma_{22\to 21}$, we observe that the Pauli exclusion within the upper-subband eventually causes a factor-of-two reduction of the scattering phase-space at $\mu_2 \approx \Delta$.

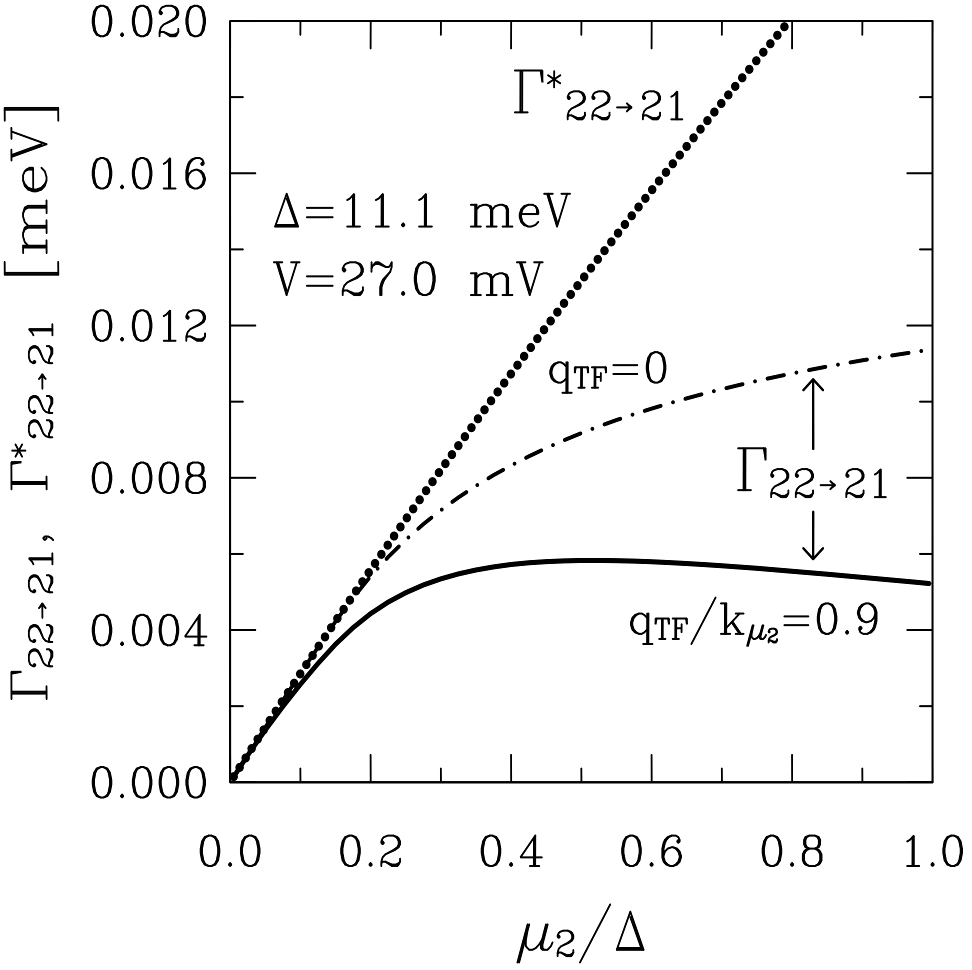

$\Gamma^*_{22\to21}$
Δ=11.1 meV
V=27.0 mV
q_{TF}=0
$\Gamma_{22\to21}$
q_{TF}/k_{μ_2}=0.9
$\Gamma_{22\to21}, \ \Gamma^*_{22\to21}$ [meV]
μ_2/Δ
0.000
0.004
0.008
0.012
0.016
0.020
0.0
0.2
0.4
0.6
0.8
1.0

FIGURE 4.3

momentum transfers, is here restricted to

$$-1 \leq q/k_{\mu_2} - \sqrt{1+(q_{\Delta/2}/k_{\mu_2})^2} \leq 1. \tag{45}$$

We observe that the phase-space contribution, Eq. (42), contains a displayed factor one half since we again only consider the opposite-spin scattering rate $\Gamma_{22\to21}$. To justify the neglect of the same-scattering we note that although the unscreened interaction matrix element, $U^0_{22,21}(q)$, will generally* diverge in the limit $q \to 0$, we find below a very moderate q-variation with the actual phase-space domain, Eq. (45), of *possible* in-plane momentum transfers q. Again we thus expect the exchange and the direct contribution to the same-spin scattering to almost cancel.

The *solid* curve in Figure 4.3 shows the estimated opposite-spin scattering rate, $\Gamma_{22\to21}$, evaluated for the effectively screened interaction defined by $U_{22,21}(q) = U^0_{22,21}(\sqrt{q^2+q_{TF}^2})$. For comparison the dashed-single-dotted curve shows the estimate rate $\Gamma_{22\to21}$ evaluated using the unscreened interaction. We note that the screening defined by the effective Thomas-Fermi wavevector, $q_{TF} \propto k_{\mu_2}$, causes at most a factor-of-two reduction also of this other nonequilibrium electron-electron scattering rate $\Gamma_{22\to21}$.

The *top* (*bottom*) panel of Figure 4.4 demonstrates that the variation with scaled momentum transfer, q/k_{μ_2}, of squared unscreened (effectively screened) matrix element, $|U^0_{22,21}(q)|^2$ ($|U_{22,21}(q)|^2 = |U^0_{22,21}(\sqrt{q^2+q_{TF}^2})|^2$) remains small at all electron occupations, μ_2/Δ. The matrix element may as a consequence be approximated by the characteristic value, $U(q_{\Delta/2} \equiv q_\Delta/\sqrt{2})$.

The *middle* panel of Figure 4.4 shows q/k_{μ_2}-variation of the weighted phase-space contribution, $(q/k_{\mu_2})P_{22\to21}(q)$. We first observe that since this contribution

* Except for strictly symmetric wavefunctions $\Psi_{1,2}(x)$.

FIGURE 4.4 Electron-occupation dependence of weighted phase-space contribution $(q/k_{\mu_2})P_{22\to21}(q)$, middle panel, *and* the unscreened (effectively screened) squared interaction matrix element, top (bottom) panel, defining scattering rate $\Gamma_{22\to21}$. The *middle* panel shows the weighted phase-space contribution, $(q/k_{\mu_2})P_{22\to21}(q)$ at different electron occupations. We find that $q_{\Delta/2} \equiv q_\Delta/\sqrt{2}$ (identified by vertical dotted line) constitute a characteristic in-plane momentum transfer in the scattering $\Gamma_{22\to21}$. We also find a μ_2/Δ-independent extension of the scattering domain, $-1 \leq 1/k_{\mu_2} - \sqrt{1+(q_{\Delta/2}/k_{\mu_2})^2} \leq 1$ for $\Gamma_{22\to21}$. *In contrast* to the scattering $\Gamma \equiv \Gamma_{22\to11}$, however, we find that the Pauli exclusion within the upper-subband reduces the scattering phase-space by as much as a factor of two at $\mu_2 \approx \Delta$. To illustrate this point, the dotted curve shows the corresponding weighted phase-space measure, $(q/k_{\mu_2})P^*_{22\to21}(q)$, evaluated at $\mu_2/\Delta = 1/2$. The *top* (*bottom*) panel demonstrates that the q/k_{μ_2}-variation of squared unscreened (effective screened) interaction matrix element $|U^0_{22,21}(q)|$ ($|U_{22,21}(q)|^2$) remains moderate at all electron occupations, μ_2/Δ, and may be approximated by the characteristic value, $|U^0_{22,21}(q_{\Delta/2})|^2$ ($|U_{22,21}(q_{\Delta/2})|^2 = |U^0_{22,21}(\sqrt{q^2_{\Delta/2}+q^2_{TF}})|^2$. However, as is evident in Figure 4.3, there is *no* approximate linear-in-μ_2 scaling of even unscreened scattering rate $\Gamma_{22\to21}$ because the integrated dimensionless phase-space measure, $I_{22\to21}(\mu_L/\Delta)$, decreases with μ_2/Δ.

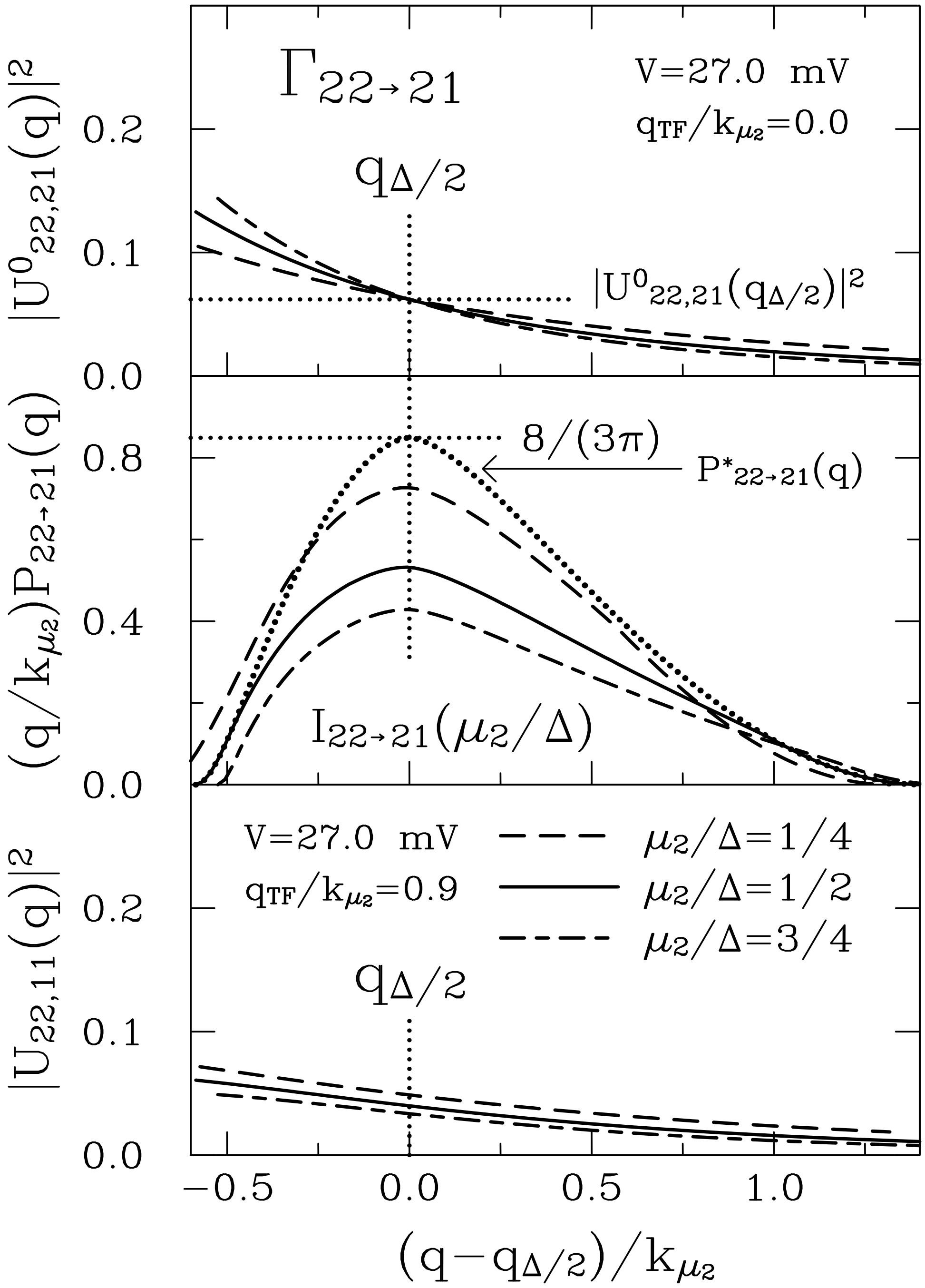

$\Gamma_{22\to21}$
V=27.0 mV
q_{TF}/k_{μ_2}=0.0
$q_{\Delta/2}$
$|U^0_{22,21}(q_{\Delta/2})|^2$
$|U^0_{22,21}(q)|^2$
8/(3π)
$P^*_{22\to21}(q)$
$(q/k_{\mu_2})P_{22\to21}(q)$
$I_{22\to21}(\mu_2/\Delta)$
V=27.0 mV
q_{TF}/k_{μ_2}=0.9
$\mu_2/\Delta=1/4$
$\mu_2/\Delta=1/2$
$\mu_2/\Delta=3/4$
$q_{\Delta/2}$
$|U_{22,11}(q)|^2$
$(q-q_{\Delta/2})/k_{\mu_2}$

FIGURE 4.4

(at relevant electron occupations, $\mu_2/\Delta < 1$,) remains peaked at the characteristic momentum transfer, Eq. (44), we may again approximate

$$\Gamma_{22\to 21} \approx \frac{\mathrm{Ry}^*}{\pi^2}\left(\frac{\mu_2}{\Delta}\right)|U_{22,21}(q_\Delta)|^2 I_{22\to 21}(\mu_2/\Delta), \tag{46}$$

with integrated phase-space measure

$$I_{22\to 21}(\mu_2/\Delta) \equiv \int \frac{dq}{k_{\mu_2}}\,\frac{q}{k_{\mu_2}} P_{22\to 21}(q). \tag{47}$$

However, the *middle* panel of Figure 4.4 also demonstrates a significant dependence on electron occupation, μ_2/Δ, of the weighted phase-space contribution, $(q/k_{\mu_2})P_{22\to 21}(q)$. and thus of the integrated phase-space measure, Eq. (47). This reduction of the phase-space measure, Eq. (42), and in particular of the integrated measure, $I_{22\to 21}(\mu_2/\Delta)$, prevents a linear-in-$\mu_2$ scaling of even the unscreened scattering rate $\Gamma_{22\to 21}$.

We emphasize that this reduction of $I_{22\to 21}(\mu_2/\Delta)$ results from Pauli exclusion within the upper-subband, see definition of scattering phase-space Eq. (42). To illustrate this point we also consider the scattering rate

$$\Gamma^*_{22\to 21} = \frac{\mathrm{Ry}^*}{\pi^2}\left(\frac{\mu_2}{\Delta}\right)\int \frac{dq}{k_{\mu_2}}|U_{22,21}(q)|^2\left[((q/k_{\mu_2})P^*_{22\to 21}(q)\right], \tag{48}$$

with dimensionless phase-space contribution $P^*_{22\to 21}(q)$, defined by

$$N_L^2\mu_2^{-1}P^*_{22\to 21}(q) = \tfrac{1}{2}\left(\frac{2}{A}\right)^2\sum_{\vec{k},\vec{k}'}\Theta(\mu_2 - E_{||}(k))\Theta(\mu_2 - E_{||}(k'))2\pi\delta(E_f - E_i), \tag{49}$$

and Eq. (43). In this modified phase-space contribution, $P^*_{22\to 21}(q)$, we do *not* require the final upper-subband state to be above μ_L unlike in Eq. (42).

The dotted curve in the middle panel of Figure 4.4 shows the weighted dimensionless phase-space measure, $(q/k_{\mu_2})P^*_{22\to 21}(q)$ at $\mu_2/\Delta = 1/2$. In complete analogy with the discussion in Section IV.B we find that weighted measure (a) is restricted to the same domain, Eq. (45), as $(q/k_{\mu_2})P_{22\to 21}(q)$, (b) is always strongly peaked at the characteristic momentum transfer, $q_{\Delta/2} \equiv q_\Delta/\sqrt{2}$, with constant peak value, $(q_{\Delta/2}/k_{\mu_2})P(q_{\Delta/2}) = 8/(3\pi)$, and consequently (c) result in an almost μ_2/Δ-independent integrated phase-space measure, $I^*_{22\to 21}(\mu_2/\Delta) \sim I_P(0)$, given by Eq. (35). We find as a consequence, an almost linear-in-μ_2 scaling of the scattering rate $\Gamma^*_{22\to 21}$ when evaluated for the unscreed interaction, (dotted curve in Figure 4.4.)

Finally, comparing in Figure 4.4 the μ_2/Δ-variation of unscreened scattering rate $\Gamma^*_{22\to 21}$ (dotted curve) and the corresponding variation of unscreened rate, $\Gamma_{22\to 21}$ (dashed-single-dotted curve,) we identify the integrated effect of the Pauli exclusion within the upper-subband. Specifically, it is clear from Figure 4.4 that the upper-subband Pauli-exclusion at $\mu_2/\Delta = 1$ causes an approximate factor-of-two reduction of the scattering rate, $\Gamma_{22\to 21}$.

IV.D The wavefunction-symmetry dependence

The *bottom* panel of Figure 4.5 shows the quantum-confined Stark effect[9] on the subband separation and on the wavefunction overlap and symmetry,[10] discussed in Section III.C. The minimal subband separation occurs at voltage drop V_{sym} (vertical dotted line,) i.e., at the avoided crossing between levels E_1 and E_2. The dipole matrix element, $|\langle\Psi_2|x|\Psi_1\rangle|$ (solid curve,) enhances only slightly with the increased wavefunction overlap at V_{sym}. In contrast, the center-of-charge separation, $\langle\Psi_2|x|\Psi_2\rangle - \langle\Psi_1|x|\Psi_1\rangle$ (dashed curve) vanishes at V_{sym} but rapidly changes with $V - V_{sym}$. This variation of the center-of-charge separation reflects, as explained in Section III.C, the loss of wavefunction-inversion symmetry.

The *top* panel of Figure 4.5 shows the corresponding dramatic voltage-drop dependence of both scattering rate Γ (solid curve) and of $\Gamma_{22\to 21}$ (dashed curve). This voltage-drop variation — evaluated for an assumed constant ratio $\mu_2/\Delta = 1/2$ — reflects the wavefunction-symmetry dependence of the characteristic intersubband Coulomb matrix elements $U(q_\Delta)$ ($U_{22,21}(q_{\Delta/2})$) which through the approximation Eq. (34) (Eq. (46)) determines Γ ($\Gamma_{22\to 21}$.) In particular, the characteristic matrix element $U(q_\Delta)$ contains an even number of upper-subband wavefunctions, can never be zero, and enhances significantly around $V \approx V_{sym}$ with the increased wavefunction overlap (as measured by the dipole matrix element.) *In contrast,* the characteristic matrix element $U_{22,21}(q_\Delta/\sqrt{2})$ contains three upper-subband wavefunctions and vanishes at $V \approx V_{sym}$ due to the restored approximate wavefunction-inversion symmetry (identified by the zero center-of-charge separation.)

In our discussion of this voltage-drop variation we first express the the general intersubband matrix element as

$$U_{ij,lk}(q) = 2\pi \int_{-\infty}^{\infty} dx_1 \int_{-\infty}^{x_1} dx_2 \frac{q_\Delta \exp(-\sqrt{q^2+q_{TF}^2}(x_1-x_2))}{\sqrt{q^2+q_{TF}^2}} \times \\ \left[\Psi_i(x_1)\Psi_j(x_1)\Psi_l(x_2)\Psi_k(x_2) + \Psi_i(x_1)\Psi_j(x_1)\Psi_l(x_2)\Psi_k(x_2)\right]. \tag{50}$$

For *symmetric* wavefunctions it follows that the only finite intersubband matrix elements, Eq. (50), contains an even number of upper- and lower-level wavefunctions.[6] Within the simple two-level description introduced in Section III.C we can then explicitly relate the variation of characteristic matrix element $U(q_\Delta)$ ($U_{22,21}(q_{\Delta/2} = q_\Delta/\sqrt{2})$) to the corresponding voltage-drop variation in the dipole matrix element (center-of-charge separation.)

FIGURE 4.5 Dramatic voltage-drop dependence (top panel) of nonequilibrium electron-electron scattering rates, Γ and $\Gamma_{22,21}$, *explained* (bottom panel) by the quantum-confined Stark effect[9] on the wavefunction overlap and symmetry. Bottom panel identifies V_{sym} (vertical dotted line) as the voltage drop with minimal subband separation (dashed-dotted curve). Observe that the dipole matrix element (solid curve) is nearly constant whereas the center-of-charge separation (dashed curve) vanishes[10] at V_{sym}. The bias dependence of Γ and $\Gamma_{22\to 21}$ reflects the wavefunction-symmetry dependence of the characteristic matrix element $|U^2(q_\Delta)|^2$ and $|U^2_{22,21}(q_{\Delta/2} = q_\Delta/\sqrt{2})|^2$, respectively. In particular, the matrix element $U(q_\Delta)$ and thus Γ enhances at V_{sym} because of the increased wavefunction overlap. In contrast, the matrix element $U_{22,21}(q_{\Delta/2}q_\Delta/\sqrt{2})$ and thus $\Gamma_{22\to 21}$ are strongly reduced close to V_{sym} but increases dramatically when, for $V \neq V_{sym}$, the wavefunction symmetry is lost. Finally, the alternating-long-short dashed curve in the top panel shows the combined electron-electron decay, $2\Gamma + \Gamma_{22\to 21}$. We emphasize the strong voltage-drop variation of also this combined decay rate which enhances to a maximum at $V = V_{sym}$ but is significantly reduced at $V \neq V_{sym}$.

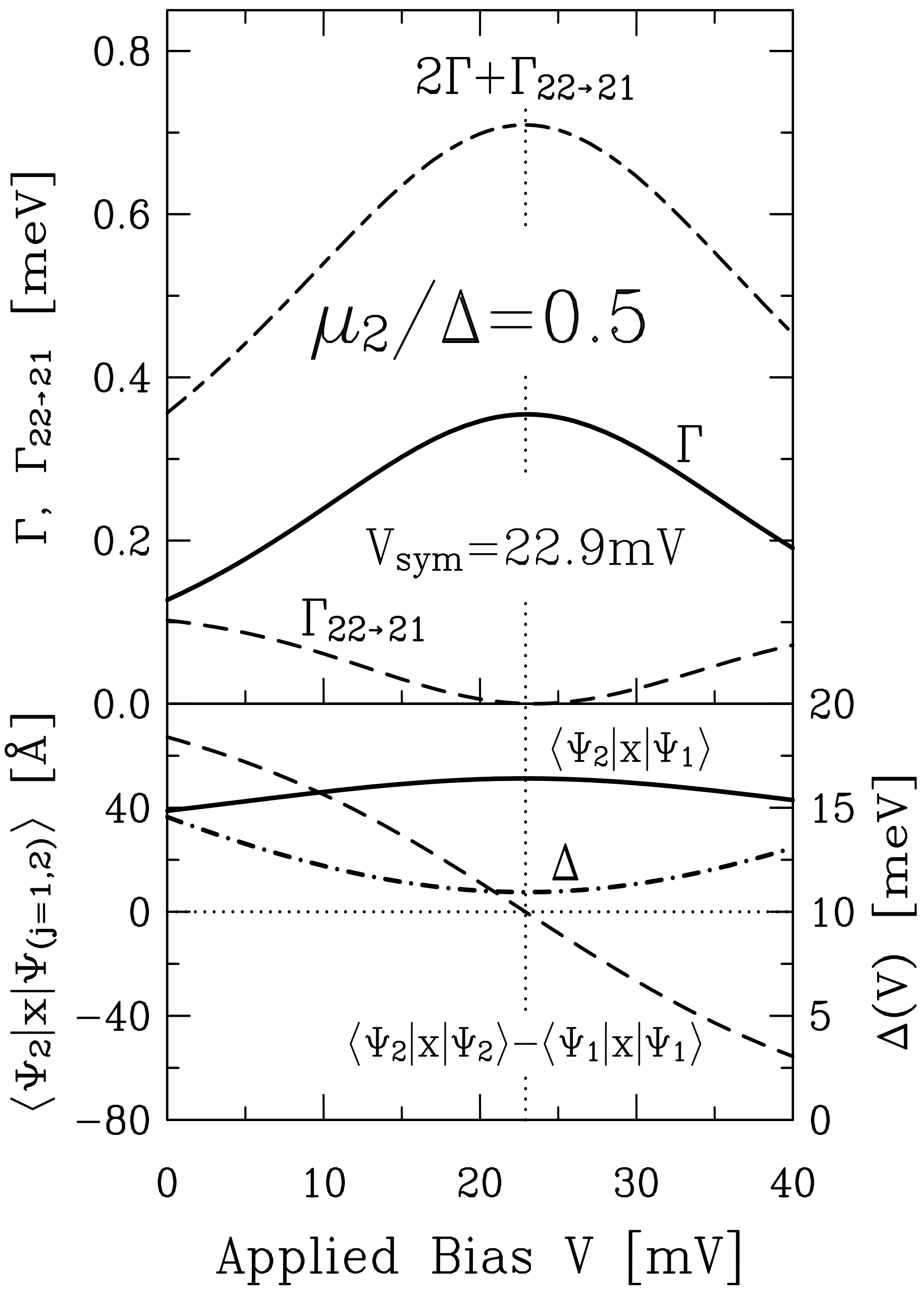
0.8
0.6
0.4
0.2
0.0
40
0
−40
−80
20
15
10
5
0
0
10
20
30
40
2Γ+Γ22→21
μ2/Δ=0.5
Γ
Vsym=22.9mV
Γ22→21
⟨Ψ2|x|Ψ1⟩
Δ
⟨Ψ2|x|Ψ2⟩−⟨Ψ1|x|Ψ1⟩
Γ, Γ22→21 [meV]
⟨Ψ2|x|Ψ(j=1,2)⟩ [Å]
Δ(V) [meV]
Applied Bias V [mV]

FIGURE 4.5

In this two-level model we assume the wavefunctions at a general voltage drop V can be expanded,

$$\Psi_2^{(V)}(x) = \cos(\chi(V - V_{sym}))\, \Psi_2^s(x) - \sin(\chi(V - V_{sym}))\, \Psi_1^s(x), \tag{51}$$

$$\Psi_1^{(V)}(x) = \sin(\chi(V - V_{sym}))\, \Psi_2^s(x) + \cos(\chi(V - V_{sym}))\, \Psi_1^s(x). \tag{52}$$

in terms of the assumed symmetric wavefunctions $\Psi_{1,2}^s(x)$ characterizing the avoided crossing, $V = V_{sym}$. The rotation angle, χ in this unitary transformation is given by

$$\tan(2\chi(V - V_{sym})) = \frac{\langle \Psi_2^s | x | \Psi_1^s \rangle}{L_{QB}} \frac{2e}{\Delta^s}(V - V_{sym}), \tag{53}$$

and varies between $-\pi/4$ (at $V \to -\infty$) over 0 (at $V = V_{sym}$) and to $+\pi/$ (in the limit $V \to \infty$,) see Section III.C. The corresponding assumed variation of the dipole matrix element and center-of-charge separation is described by

$$\langle \Psi_2^{(V)} | x | \Psi_1^{(V)} \rangle = \cos(2\chi(V - V_{sym})) \langle \Psi_2^s | x | \Psi_1^s \rangle, \tag{54}$$

and

$$\langle \Psi_2^{(V)} | x | \Psi_2^{(V)} \rangle - \langle \Psi_1^{(V)} | x | \Psi_1^{(V)} \rangle = -2 \sin(2\chi(V - V_{sym})) \langle \Psi_2^s | x | \Psi_1^s \rangle. \tag{55}$$

Consider first the significant variation of characteristic intersubband matrix element $U(q_\Delta)$. We assume that the wavefunctions $\Psi_{1,2}^s(x)$ at $V = V_{sym}$ are exactly symmetric and denote by $U_{21,21}^s(q)$ the value of the matrix element $U(q)$ at $V = V_{sym}$. We approximate the matrix element at a general voltage drop V by inserting the two-level wavefunctions $\Psi_{1,2}^{(V)}(x)$ in for $\Psi_{i=k=2/j=l=1}(x)$ in Eq. (50).

Within the approximate two-level description the limit $V \to \infty$ is described by upper- (lower)-level wavefunction $\Psi_L(x)$ ($\Psi_R(x)$) concentrated in the left (right) quantum well and given by

$$\Psi_2^{(\infty)}(x) = \Psi_L(x) \equiv \left[\Psi_2^s(x) - \Psi_1^s(x)\right]/\sqrt{2}, \tag{56}$$

$$\Psi_1^{(\infty)}(x) = \Psi_R(x) \equiv \left[\Psi_2^s(x) + \Psi_1^s(x)\right]/\sqrt{2}. \tag{57}$$

These wavefunction does have a small but finite wavefunction overlap resulting in a non-zero matrix element

$$U_{12,12}^{(\infty)}(q) = U_{LR,LR}(q), \tag{58}$$

given by inserting the wavefunctions $\Psi_{R/L}(x)$ for $\Psi_{i=k=1/j=l=2}(x)$ in Eq. (50). At a general voltage-drop V the approximate matrix element can now be expressed

$$\begin{aligned} U_{12,12}^{(V)}(q) &= \cos^2(2\chi(V - V_{sym}))U_{12,12}^s(q) + \sin^2(2\chi(V - V_{sym}))U_{LR,LR}(q), \\ &= U_{LR,LR}(q) + \cos^2(2\chi(V - V_{sym}))(U_{12,12}^s(q) - U_{LR,LR}(q)). \end{aligned} \tag{59}$$

The assumed behavior, $U_{12,12}^{(V)}(q) \to U_{LR,LR}(q)$ in the limit $V \to \infty$ must be considered an artifact of the two-level description. However, we expect Eq. (59) to provide the correct voltage-drop dependence around around $V = V_{sym}$, and note that the value $U_{LR,LR}$ can instead be expresses directly in terms of the actual matrix elements at $V = V_{sym}$:

$$U_{LR,LR}(q) = \left[U_{22,22}^s(q) + U_{11,11}^s(q) - 2U_{11,22}^s(q)\right]/4. \tag{60}$$

In particular, we conclude based on Eq. (59), that the significant voltage-drop variation of characteristic matrix element $U(q_\Delta)$ evident in Figure 4.5 results directly from the moderate variation of the dipole matrix element, Eq. (54).

For the intersubband matrix element $U_{12,22}^{(V)}(q)$ (similarly given by inserting the two-level wavefunctions $\Psi_{1,2}^{(V)}(x)$ in Eq. (50)) it clear that

$$U_{22,21}^s(q) \equiv 0, \tag{61}$$

because of the assumed symmetry at V_{sym}. For a general voltage drop V we expand the two-level wavefunctions $\Psi^{(V)}_{1,2}(x)$ in terms of $\Psi^{s}_{1,2}(x)$ and obtain an approximate matrix element,

$$U^{(V)}_{22,21}(q) \propto \sin(2\chi(V - V_{sym})), \tag{62}$$

proportional to the center-of-charge separation. It follows in particular that the actual characteristic intersubband matrix element, $U_{22,21}(q = q_{\Delta/2} = q_{\Delta}/\sqrt{2})$, must vanish at a bias $V = V'_{sym} \approx V_{sym}$. Although the condition, $U_{22,21}(q = q_{\Delta/2}) = 0$, does not of course ensure that the general matrix element, $U_{22,21}(q)$, vanishes at $V = V'_{sym}$, the quantum-confined Stark effect[9] on the wavefunction symmetry[10] in $U_{22,21}(q)$ does cause a more than six orders of magnitude of scattering rate $\Gamma_{22\to 21}$ around $V = V_{sym}$.

Finally, we observe that the dramatic voltage-drop/wavefunction-symmetry variation of the intersubband Coulomb matrix elements $U(q)$ and $U_{12,22}(q)$ also causes an strong variation in the *total* nonequilibrium electron-electron intersubband decay. This follows because a scattering event (unlike $\Gamma_{22\to 21}$) removes *both* upper-subband electrons to the lower subband and the total decay is thus given by $2\Gamma + \Gamma_{22\to 21}$. The alternating-long-short-dashed curve in the top panel of Figure 4.5 shows the variation of this combined decay rate, $2\Gamma + \Gamma_{22\to 21}$, which enhances to a maximum at $V = V_{sym}$ but is significantly reduced at $V \neq V_{sym}$.

IV.E The finite intersubband population inversion

Thanks to the above study of the nonequilibrium electron-electron scattering we are now able to estimate the total intersubband decay and resulting population inversion, the main focus of this dissertation. We provide this estimate at the avoided crossing, $V = V_{sym}$, where the combined electron-electron decay, $\sim 2\Gamma + \Gamma_{22\to 21}$, enhances to a maximum as demonstrated in Figure 4.5.

We denote the upper- and lower-subband occupation density by n_2 and n_1, respectively. Using the two-level rate equation introduced in Section I.D:

$$\begin{aligned} \frac{dn_2}{dt} &= (N_L - n_2)\Gamma_e - n_2\Gamma_{c2} - n_2\Gamma_{nr}(n_2), \\ \frac{dn_1}{dt} &= n_2\Gamma_{nr}(n_2) - n_1\Gamma_{c1}, \end{aligned} \tag{63}$$

and a simple assumption,

$$\Gamma_{nr}(n_2) = \Gamma_{sp} + 2\left(\frac{n_2}{N_L}\right) \mathrm{Ry}^* \left(\frac{\mu_2}{\Delta}\right) |U^0(q_\Delta)|^2 I_P(0), \tag{64}$$

for the total intersubband decay rate we furthermore determine the resulting inter-subband population inversion, $n_2 - n_1$, and current densities, $J = e\Gamma_e(N_L - n_2)$. These estimates for the population inversion and current densities are shown in the *bottom* panel of Figure 4.6, left and right axis, respectively.

The rate equation, Eq. (63), involves tunneling the tunneling rates Γ_e, Γ_{c1} and Γ_{c2} illustrated in Figure 1.1 and estimated in Section III.D. We may assume[17] the total *single*-electron decay rate (Γ_{se}) experimentally bounded by the value, $1/\tau \approx$ 0.03 meV, measured[2] at weak optical pumping and at temperatures $T \leq 50$ K.

The *top* panel of Figure 4.6 shows the μ_2/Δ-dependence at $V = V_{sym}$ of the electron-electron scattering rates — evaluated for a complete upper-subband occupation below the emitter chemical potential, $\mu_L \equiv E_2 + \mu_2$. The estimate, $\Gamma_{nr}(n_2) - \Gamma_{se}$, for the total decay due to the electron-electron scattering at $V = V_{sym}$ and a *partial* current-injected upper-subband occupation, $n_2 \leq N_L$, results as follows. The scattering $\Gamma_{22\to 12}$ (shown by dotted curve in top panel) can be

FIGURE 4.6 *Top* panel shows the approximate scaling, solid curve, with electron occupation, μ_2/Δ, of unscreened (screened) nonequilibrium scattering rate Γ, dashed-single(double)-dotted curve. Screening causes at most a factor of two reduction of Γ even at $\mu_2 = \Delta$. The interaction matrix elements are evaluated at V_{sym} where the rate $\Gamma_{22\to 21}$, dotted curve, essentially vanishes. *Bottom* panel demonstrates that a finite population inversion (left axis) $n_2 - n_1 \sim 0.17 \times 10^{11}$ cm^{-2} can be maintained at a moderate current density (right axis) $J = e\Gamma_e(N_L - n_2)$ in spite of the strong intersubband scattering. Note, however, that the population inversion quickly saturates and eventually decreases whereas the current density $J = eN_L(1 - n_2/N_L)$ shows a faster-than-linear increase with μ_2/Δ.

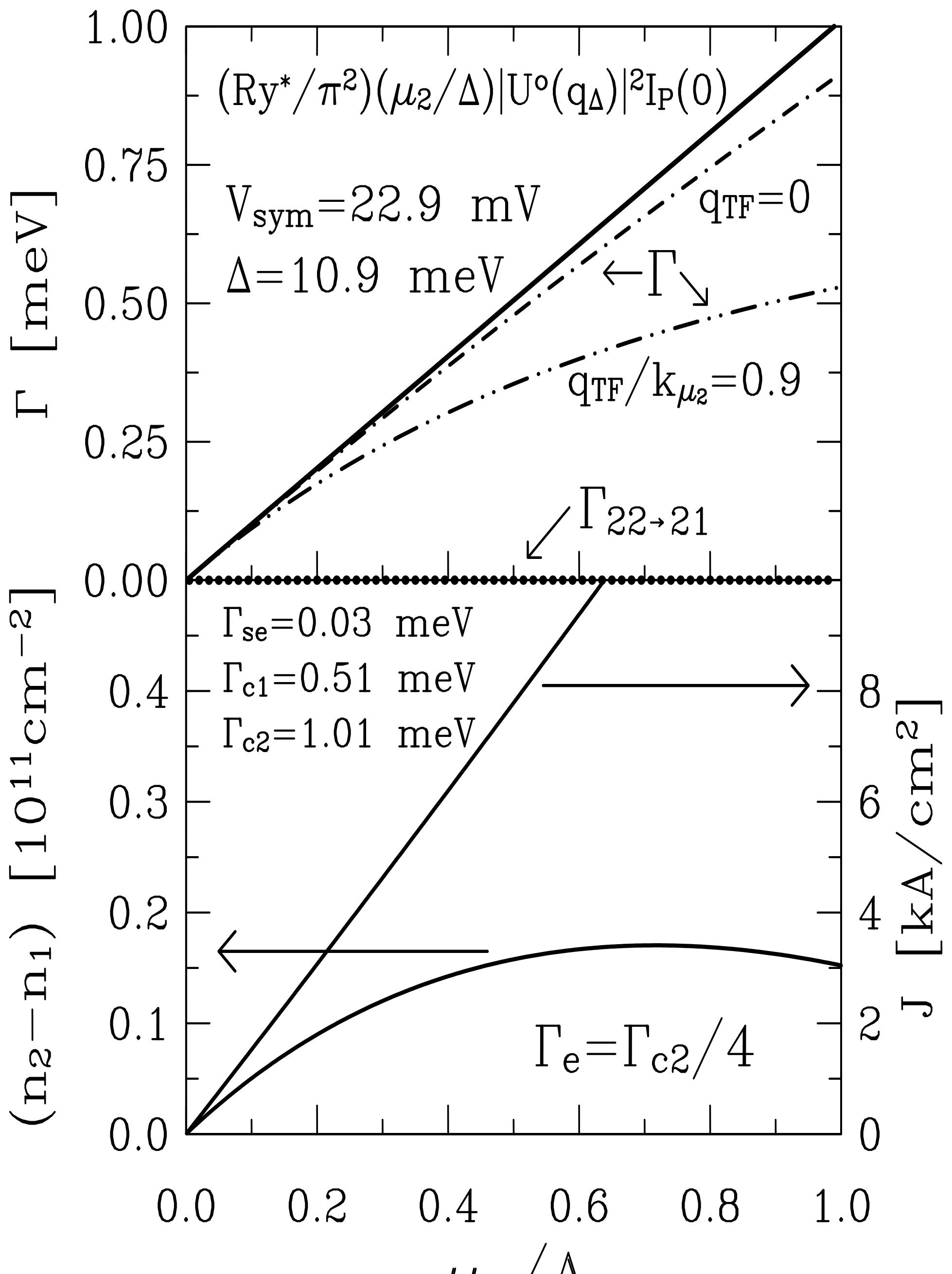
(Ry*/π²)(μ₂/Δ)|U°(q_Δ)|²I_P(0)
V_sym=22.9 mV
Δ=10.9 meV
q_TF=0
←Γ↘
q_TF/k_μ₂=0.9
Γ_22→21
Γ_se=0.03 meV
Γ_c1=0.51 meV
Γ_c2=1.01 meV
Γ_e=Γ_c2/4
Γ [meV]
(n₂−n₁) [10¹¹cm⁻²]
J [kA/cm²]
μ₂/Δ
1.00
0.75
0.50
0.25
0.00
0.4
0.3
0.2
0.1
0.0
0.2
0.4
0.6
0.8
1.0
8
6
4
2
0

FIGURE 4.6

neglected at V_{sym} due to the restored wavefunction-inversion symmetry (Section IV.D.) The scattering Γ does remove two electrons at a time but is reduced by the partial upper-subband occupation, $n_2 \leq N_L$. For simplicity we assume this partial upper-subband occupation is distributed according to

$$f_2(k) \equiv (n_2/N_L) \times \Theta(\mu_2 - E_{||}(k)). \tag{65}$$

Finally, we approximate the resulting electron-electron decay $2(n_2/N_L)\Gamma$ using the scaling approximation (solid curve in top panel) for the unscreened rate Γ.

The current-injection in the mid-infrared quantum cascade laser[11,12,13] maintains a population inversion $n_2 - n_2 \approx n_2 \approx N_L \sim 10^{11}$ cm^{-2} which requires $\mu_2 \approx 5$ meV and $\Gamma_e \gg \Gamma_{c2}$. In the present far-infrared structure, however, the resulting strong scattering scattering, $\Gamma \approx 0.5$ meV, will eliminate such a population inversion. Nevertheless, the estimates reported in the *bottom* panel of Figure 4.6 demonstrates that a smaller population inversion, $n_2 - n_1 \approx 0.17 \times 10^{11}$ cm^{-2} *can* be maintained at current densities comparable those in the mid-infrared quantum cascade laser.[11,12,13]

These estimates are given by the steady-state solutions of the rate equation, Eq. (63). Specifically estimate at the avoided crossing, $V = V_{sym}$ the upper-subband population density at

$$\frac{n_2}{N_L} = \frac{(\Gamma_e + \Gamma_{c2} + \Gamma_{se})}{4\Gamma} \left[\sqrt{1 + 8\frac{\Gamma\Gamma_e}{(\Gamma_e + \Gamma_{c2} + \Gamma_{se})^2}} - 1 \right], \tag{66}$$

which in particular determines the current density

$$J = e\Gamma_e N_L (1 - \frac{n_2}{N_L}). \tag{67}$$

For the resulting population inversion we find

$$\frac{n_2 - n_1}{N_L} = -\frac{\Gamma_e}{\Gamma_c 1} + \frac{(\Gamma_e + \Gamma_{c2} + \Gamma_{c1})(\Gamma_e + \Gamma_{c2} + \Gamma_{se})}{4\Gamma\Gamma_{c1}} \times \left[\sqrt{1 + 8\frac{\Gamma\Gamma_e}{(\Gamma_e + \Gamma_{c2} + \Gamma_{se})^2}} - 1\right]. \tag{68}$$

The bottom panel of Figure 4.6 shows these estimate for the population inversion density and current density evaluated at the specified[18] tunneling rates.

We emphasize that this estimated population inversion, $n_2 - n_1$, as shown in Figure 4.6, quickly saturates and eventually decreases whereas the current density, $J = e\Gamma_e N_L(1 - n_2/N_L)$, shows a faster-than-linear increase with μ_2/Δ. A choice of $\Gamma_e \sim \Gamma_{c2} \approx 1.0$ meV (not shown) does not increase the maximum population inversion and causes a strongly nonlinear rise of the current with μ_2/Δ. Hence, the electron-electron scattering forces a nontrivial optimization of Γ_e/Γ_{c2} and μ_2/Δ.

Finally, we reiterate that we have above estimated the resulting intersubband population inversion at the avoided crossing $V = V_{sym}$ and using the scaling result for the unscreened rate Γ. At this avoided crossing the combined electron-electron decay (given by $2\Gamma + \Gamma_{22\to 21}$) enhances to a maximum as shown in the top panel of Figure 4.5. Hence, we have above *overestimated* the effect the intersubband electron-electron scattering. It should thus be possible to increase the population inversion (beyond the value $n_2 - n_1 \approx 0.17 \times 10^{11}$ cm^{-2}, reported in Figure 4.6) by ensuring a strong upper-subband current injection at a voltage drop $V \neq V_{sym}$ where the wavefunction-inversion symmetry is lost and the combined electron-electron decay is significantly reduced.

REFERENCES

1. J. N. Heyman, K. Craig, B. Galdrikian, M. S. Sherwin, K. Campman, P. F. Hopkins, S. Fafard, and A. C. Gossard, *Phys. Rev. Lett.* **72**, 2183 (1994).

2. J. N. Heyman, K. Unterrainer, K. Craig, B. Galdrikian, M. S. Sherwin, K. Campman, P. F. Hopkins, A. C. Gossard, *Phys. Rev. Lett.* **74**, 2682 (1995). The experimentally investigated isolated quantum-well sample constitute the central region of the Figure 1.1-tunneling structure.

3. Reference 2 also report a moderate decay rate ($1/\tau \approx 0.05$ meV at $T = 10$ K) under a strong optical pumping. A comparison requires, however, a detailed modeling of the optically excited electron gas and is not presently undertaken.

4. S. J. Allen, Jr., D. C. Tsui, and B. Vinter, *Solid State Comm.* **20**, 425 (1976).

5. T. Ando, A. B. Fowler, and F. Stern, *Rev. Mod. Phys.* **54**, 437 (1982); see pp. 473–476.

6. Q. P. Li and S. Das Sarma, *Phys. Rev. B* **43**, 11768 (1991); Ben Yu-Kuang Hu and S. Das Sarma, *Phys. Rev. B* **48**, 5469 (1993).

7. M. Zaluzny, *Phys. Rev. B* **47**, 3995 (1993); *J. Appl. Phys.* **74**, 4716 (1993).

8. V. I. Fal'ko, *Phys. Rev. B* **47**, 13585 (1993); P. Sotirelis, *Phys. Rev. B* **47**, 12744 (1993).

9. D. A. B. Miller, D. S. Chelma, T. C. Damen, A. C. Gossard, W. Wiegmann, T. H. Wood, and C. A. Burrus, *Phys. Rev. Lett.* **53**, 2173 (1984).

10. J. Faist, F. Capasso, A. L. Hutchinson, L. Pfeiffer, and K. W. West, *Phys. Rev. Lett.* **71**, 3573 (1993); this paper reports and explains the corresponding voltage-drop dependence of the optical selection rules.

11. J. Faist, F. Capasso, D. L. Sivco, C. Sirtori, A. L. Hutchinson, and A. Y. Cho, *Science* **264**, 553 (1994).

12. J. Faist, F. Capasso, D. L. Sivco, C. Sirtori, A. L. Hutchinson, and A. Y. Cho, *Electronics Letters* **30**, 865–866 (1994).

13. J. Faist, F. Capasso, D. L. Sivco, A. L. Hutchinson, C. Sirtori, S. N. G. Chu, and A. Cho, *Appl. Phys. Lett.* **65**, 2901 (1994).

14. We thank Dr. B. Galdrikian for kind permission to use his Schrödinger-solver code.

15. The rate Γ is defined as the total rate of scattering between two upper-subband electrons which both decay to subband E_1 — *per* upper-subband electron assuming a complete upper-subband occupation, i.e., $n_2 = N_L$. For an area A the total number of upper-subband electrons is thus AN_L and we have $\{AN_L\}\Gamma \equiv \sum_{\vec{q}}(e^2/\epsilon_0 q_\Delta)^2|U(q)|^2 N_L^2 \mu_2^{-1} P(q)$ with phase-space contribution $N_L^2 \mu_2^{-1} P(q)$ listed in Eq. (31).

16. The rate $\Gamma_{22\to 21}$ is defined as the total rate of scattering between two upper-subband electrons of which only one decays to subband E_1 — again *per* upper-subband electron assuming a complete upper-subband occupation, i.e., $n_2 = N_L$, and respecting the Pauli exclusion within the upper-subband. For an area A the total number of upper-subband electrons is again AN_L and we have $\{AN_L\}\Gamma_{22\to 21} \equiv \sum_{\vec{q}}(e^2/\epsilon_0 q_\Delta)^2|U_{22,21}(q)|^2 N_L^2 \mu_2^{-1} P_{22\to 21}(q)$ with phase-space contribution $N_L^2 \mu_2^{-1} P_{22\to 21}(q)$ listed in Eq. (42).

17. The intersubband decay due to impurity, interface defect and acoustic phonon scattering remains at temperatures $T \leq 50$ K strictly bounded by the experimental value $1/\tau = 0.03$ meV. We estimate the decay due to thermally activated optical-phonon emission bounded at 10^{-3} meV for $T \leq 25$ K.

18. We take in this evaluation $\Gamma_{c1(c2)} = 0.51(1.01)$ meV (estimated in Section I.D at the avoided crossing $V = V_{sym}$) and use $\Gamma_e = \Gamma_{c2}/4$.